Advances in Applied Mathematics and Mechanics
Adv. Appl. Math. Mech., Vol. **8**, No. 2, pp. 236-256

DOI: 10.4208/aamm.2014.m459
April 2016

Noise Prediction in Subsonic Flow Using Seventh-Order Dissipative Compact Scheme on Curvilinear Mesh

Meiliang Mao[1,3], Yi Jiang[1,3,*], Xiaogang Deng[2] and Huayong Liu[1]

[1] *State Key Laboratory of Aerodynamics, China Aerodynamics Research and Development Center, P.O. Box 211, Mianyang 621000, China*
[2] *National University of Defense Technology, Changsha 410073, China*
[3] *Computational Aerodynamics Institute, China Aerodynamics Research and Development Center, P.O. Box 211, Mianyang 621000, China*

Received 6 January 2014; Accepted (in revised version) 31 December 2014

Abstract. In this paper, we investigate the performance of the seventh-order hybrid cell-edge and cell-node dissipative compact scheme (HDCS-E8T7) on curvilinear mesh for noise prediction in subsonic flow. In order to eliminate the errors due to surface conservation law (SCL) is dissatisfied on curvilinear meshes, the symmetrical conservative metric method (SCMM) is adopted to calculate the grid metric derivatives for the HDCS-E8T7. For the simulation of turbulence flow which may have main responsibility for the noise radiation, the new high-order implicit large eddy simulation (HILES) based on the HDCS-E8T7 is employed. Three typical cases, i.e., scattering of acoustic waves by multiple cylinder, sound radiated from a rod-airfoil and subsonic jet noise from nozzle, are chosen to investigate the performance of the new scheme for predicting aeroacoustic problem. The results of scattering of acoustic waves by multiple cylinder indicate that the HDCS-E8T7 satisfying the SCL has high resolution for the aeroacoustic prediction. The potential of the HDCS-E8T7 for aeroacoustic problems on complex geometry is shown by the predicting sound radiated from a rod-airfoil configuration. Moreover, the subsonic jet noise from nozzle has been successfully predicted by the HDCS-E8T7.

AMS subject classifications: 76Fxx, 76Qxx
Key words: Aeroacoustics, seventh-order hybrid cell-edge and cell-node dissipative compact scheme (HDCS-E8T7), high-order implicit large eddy simulation (HILES), symmetrical conservative metric method (SCMM), complex geometry.

1 Introduction

Aeroacoustic problem is serious in many engineering applications. It can cause human discomfort and affect the stealth operations of military air vehicles and submarines [1].

*Corresponding author.
Email: yijiang@mail.ustc.edu.cn (Y. Jiang)

 ©2016 Global Science Press

https://doi.org/10.4208/aamm.2014.m459 Published online by Cambridge University Press

Accordingly, the aeroacoustic noise reduction is an important goal for the commercial and military aviation communities [2]. For evaluation of the performance of the new noise-reducing concepts, reliable methods for modeling of the source mechanisms must be available. However, the nature of aeroacoustic problems is essentially different from that of standard aerodynamic problems [3]. To be able to compute or simulate aeroacoustics problems accurately and efficiently, a computational aeroacoustics (CAA) scheme should have extremely low dispersion and dissipation errors [3]. Traditional second order accurate methods are known to be too dissipative for these problems. Due to the high formal order, good spectral resolution and their flexibility, high-order compact finite difference schemes are the most attractive schemes for CAA [4]. CAA based on high-order compact finite difference scheme has been applied successfully to various aerodynamic noise problems. For example, noise generated by jet flow has been successfully predicted via the direct noise computation approach [5], i.e., simulation of both the unsteady flow and the associated sound should be performed in the same computation [6]. Based on the sixth-order central compact finite difference scheme proposed by Lele [7], noise radiated by wake-airfoil interaction, which helps to understand the mechanism of acoustic radiation in turbo-machine, has been studied [8]. This sixth-order compact scheme is also used by Rizzetta et al. [9] to investigate acoustic suppression of cavity flow.

In order to provide more realistic aeroacoustic prediction, applications of high-order compact finite difference schemes are motivated to increasingly complex configurations of engineering interest. However, applications of these schemes are still challenged by complex meshes which are commonly used for complex geometry. When the accurate numerical simulation of broad spectrum phenomenon is performed by high-order compact scheme on a complex mesh, it is argued that there are many obstacles such as robustness and grid-quality sensitivity [10, 11]. Fortunately, these deficiencies can be largely removed by the researches of the Geometric Conservation Law (GCL) [12–16]. The GCL contains surface conservation law (SCL) and volume conservation law (VCL). The VCL has been widely studied for time-dependent grids, while the SCL is merely discussed for finite difference schemes. If the SCL has not been satisfied, numerical instabilities and even computing collapse may appear on complex curvilinear grids during numerical simulation. In order to fulfill the SCL for high-order finite difference schemes, the conservative metric method (CMM) is derived by Deng et al. [15]. The CMM is achieved by computing grid metric derivatives through a conservative form with the same scheme applied to fluxes. According to the principle of satisfying the CMM, the seventh-order hybrid cell-edge and cell-node dissipative compact scheme (HDCS-E8T7) has been proposed for simulating subsonic flow on complex geometry [17]. The advantages of the HDCS-E8T7 are: (a) it can satisfy the GCL which helps to preserve the accuracy orders on curvilinear meshes, and enhances the ability of the HDCS-E8T7 to handle complex geometry; (b) it has inherent dissipation which is quite useful in dissipating unresolvable wavenumbers; (c) high-order accuracy can be obtained in relatively narrow stencils, thus the boundary and near boundary schemes are easily designed, and the HDCS-E8T7 can be applied on complex multi-block structured grid conveniently. The properties of

https://doi.org/10.4208/aamm.2014.m459 Published online by Cambridge University Press

the HDCS-E8T7 scheme have been systemically analyzed by Deng et al. [18]. Besides the GCL, multi-block structured grid technique may be another requirement for the applications of high-order finite difference schemes on complex geometries, because it is difficult to generate a single-block structured grid system for a complex configuration. The Characteristic-Based Interface Conditions (CBIC) in [19] and the nonlinear patched grid method in [20] are quite useful in handling multi-block structured grids, so as to enable the use of high-order schemes on complex geometries.

For the prediction of noise radiated by turbulent flow, LES may be a satisfying choice according to currently available computer resources [5]. Based on the HDCS-E8T7, the high-order implicit LES (HILES) is proposed by Jiang et al. [21]. Although the concept of the HILES is same as that of monotone integrated LES (MILES) [22], i.e., the effects of explicit LES models are imitated by the truncation error of the discretization scheme itself, the HDCS-E8T7 for the HILES is a new seventh-order dissipative compact scheme which can satisfy the SCL and has inherent dissipation. Due to the inherent dissipation, numerical dissipation of the HILES is introduced by the HDCS-E8T7 itself. For the applications of the HILES on curvilinear meshes, a very important feature of the HDCS-E8T7 is that it can satisfy the SCL, because the computation of the HILES may be contaminated or even collapse when the SCL is not satisfied. On the other hand, the ability of the HILES in handling complex geometry is enhanced if the SCL errors are eliminated [23, 24]. To enable the use of the HILES on complex geometry, a special sixth-order interface scheme is proposed to avoid grid singularity [25]. Moreover, the HILES based on the HDCS-E8T7 has been used to predict the stall phenomenon successfully [21], and it is expected to be a suitable method for simulating the unsteady turbulence flow on curvilinear meshes.

The objective of the present work is to investigate the performance of the HDCS-E8T7 on curvilinear meshes for the aeroacoustic prediction in subsonic flow. Three typical cases are chosen for this investigation. The first one is the scattering of acoustic waves by multiple cylinder. High resolution of the HDCS-E8T7 for aeroacoustic prediction on curvilinear mesh will be observed in this test. The second one is sound radiated by a rod-airfoil configuration. This test is employed to demonstrate the potential of the HDCS-E8T7 for aeroacoustic noise prediction on complex geometry. The last one is jet noise from nozzle. We will examine the ability of the HDCS-E8T7 for prediction of jet noise which is a major source of noise radiated from the aircraft, particularly during takeoff and landing. In the next section, the governing equations are given. In Section 3, numerical methods for the aeroacoustic prediction are given. Numerical results are presented in Section 4.

2 Governing equations

Three dimensional Navier-Stokes equations in computational coordinates may be written as

$$\frac{\partial \widetilde{U}}{\partial t}+\frac{\partial \widetilde{E}}{\partial \xi}+\frac{\partial \widetilde{F}}{\partial \eta}+\frac{\partial \widetilde{G}}{\partial \zeta}=\frac{\theta}{R_e}\left(\frac{\partial \widetilde{E}_v}{\partial \xi}+\frac{\partial \widetilde{F}_v}{\partial \eta}+\frac{\partial \widetilde{G}_v}{\partial \zeta}\right)+\frac{\overrightarrow{S}}{J}, \tag{2.1}$$

https://doi.org/10.4208/aamm.2014.m459 Published online by Cambridge University Press

where $\theta=1$ for Navier-Stokes equations, and $\theta=0$ for Euler equations, $\overrightarrow{S}$ is a source term, and it is non-zero only for the computation of scattering of acoustic waves by multiple cylinders (Subsection 4.1) in this paper,

$$\begin{aligned}
&\widetilde{U}=U/J,\\
&\widetilde{E}=(\xi_t U+\xi_x E+\xi_y F+\xi_z G)/J, \qquad &&\widetilde{E}_v=(\xi_x E_v+\xi_y F_v+\xi_z G_v)/J,\\
&\widetilde{F}=(\eta_t U+\eta_x E+\eta_y F+\eta_z G)/J, \qquad &&\widetilde{F}_v=(\eta_x E_v+\eta_y F_v+\eta_z G_v)/J,\\
&\widetilde{G}=(\varsigma_t U+\zeta_x E+\zeta_y F+\zeta_z G), \qquad &&\widetilde{G}_v=(\zeta_x E_v+\zeta_y F_v+\zeta_z G_v)/J,
\end{aligned}$$

and

$$\begin{aligned}
&U=[\rho,\rho u,\rho v,\rho w,\rho e]^T,\\
&E=\left[\rho u,\rho u^2+p,\rho vu,\rho wu,(\rho e+p)u\right]^T,\\
&F=\left[\rho v,\rho uv,\rho v^2+p,\rho wv,(\rho e+p)v\right]^T,\\
&G=\left[\rho w,\rho uw,\rho vw,\rho w^2+p,(\rho e+p)w\right]^T,\\
&E_v=\left[\ 0,\quad \tau_{xx},\quad \tau_{xy},\quad \tau_{xz},\quad u\tau_{xx}+v\tau_{xy}+w\tau_{xz}+\dot{q}_x\ \right]^T,\\
&F_v=\left[\ 0,\quad \tau_{yx},\quad \tau_{yy},\quad \tau_{yz},\quad u\tau_{yx}+v\tau_{yy}+w\tau_{yz}+\dot{q}_y\ \right]^T,\\
&G_v=\left[\ 0,\quad \tau_{zx},\quad \tau_{zy},\quad \tau_{zz},\quad u\tau_{zx}+v\tau_{zy}+w\tau_{zz}+\dot{q}_z\ \right]^T,
\end{aligned}$$

with viscous stress terms written as

$$\tau_{ij}=\mu\Big(\frac{\partial u_i}{\partial x_j}+\frac{\partial u_i}{\partial x_j}-\frac{2}{3}\delta_{ij}\frac{\partial u_l}{\partial x_l}\Big),$$

and heat transfer terms

$$\dot{q}_x=\frac{1}{(\gamma-1)P_rM_\infty^2}\mu\frac{\partial T}{\partial x},\quad \dot{q}_y=\frac{1}{(\gamma-1)P_rM_\infty^2}\mu\frac{\partial T}{\partial y},\quad \dot{q}_z=\frac{1}{(\gamma-1)P_rM_\infty^2}\mu\frac{\partial T}{\partial z},$$

where γ is the ratio of specific heats, and the viscous coefficient μ can be calculated by the Sutherland's law. The equation of state and the energy function are

$$p=\frac{1}{\gamma M^2}\rho T,\quad e=\frac{p}{(\gamma-1)\rho}+\frac{u^2+v^2+w^2}{2}.$$

In the above u, v and w are the velocity components in x, y and z directions, respectively, p is the pressure, ρ is the density and T is temperature. The non-dimensional variables are defined as $\rho=\rho^*/\rho_\infty^*$, $(u,v,w)=(u,v,w)^*/V_\infty^*$, $T=T^*/T_\infty^*$, $p=p^*/\rho_\infty^*V_\infty^{*2}$, $\mu=\mu^*/\mu_\infty^*$ respectively, and $M_\infty=u_\infty/\sqrt{\gamma RT_\infty^*}$, $R_e=\rho_\infty^*u_\infty^*r^*/\mu_\infty^*$, $P_r=\mu_\infty^*C_p/\kappa_\infty^*$ are the Mach number, Reynolds number and Prandtl number, r^* is the characteristic length. J is the Jacobi

https://doi.org/10.4208/aamm.2014.m459 Published online by Cambridge University Press

of grid transformation, ξ_t, ξ_x, ξ_y, ξ_z, η_t, η_x, η_y, η_z, ζ_t, ζ_x, ζ_y, ζ_z are grid derivatives. The grid metric derivatives have the conservative form as

$$\begin{cases} \tilde{\xi}_x=\dfrac{\xi_x}{J}=(y_\eta z)_\zeta-(y_\zeta z)_\eta, & \tilde{\xi}_y=\dfrac{\xi_y}{J}=(z_\eta x)_\zeta-(z_\zeta x)_\eta, & \tilde{\xi}_z=\dfrac{\xi_z}{J}=(x_\eta y)_\zeta-(x_\zeta y)_\eta, \\ \tilde{\eta}_x=\dfrac{\eta_x}{J}=(y_\zeta z)_\xi-(y_\xi z)_\zeta, & \tilde{\eta}_y=\dfrac{\eta_y}{J}=(z_\zeta x)_\xi-(z_\xi x)_\zeta, & \tilde{\eta}_z=\dfrac{\eta_z}{J}=(x_\zeta y)_\xi-(x_\xi y)_\zeta, \\ \tilde{\zeta}_x=\dfrac{\zeta_x}{J}=(y_\xi z)_\eta-(y_\eta z)_\xi, & \tilde{\zeta}_y=\dfrac{\zeta_y}{J}=(z_\xi x)_\eta-(z_\eta x)_\xi, & \tilde{\zeta}_z=\dfrac{\zeta_z}{J}=(x_\xi y)_\eta-(x_\eta y)_\xi. \end{cases} \tag{2.2}$$

3 Numerical methods

3.1 Spatial discretization

Seventh-order finite difference scheme HDCS-E8T7 is employed for the HILES to discretize the Eq. (2.1). The HDCS-E8T7 is proposed by developing the dissipative compact scheme (DCS) [26] for simulating subsonic flow on complex geometry. Although the DCS has successfully simulated some aeroacoustic benchmark problems [27–30], applications of the DCS on complex grids may have serious problem [15]. The HDCS-E8T7 has demonstrated the promising ability in solving complex flow problems, moreover, the accuracy orders of the HDCS-E8T7 have been preserved on curvilinear meshes because the SCL is satisfied [18]. For the convenience of understanding our high-order strategy for the noise prediction, details of the HDCS-E8T7 will be given in the following.

Considering discretization of the inviscid terms,

$$\frac{\partial\widetilde{U}}{\partial t}+\frac{\partial\widetilde{E}}{\partial\xi}+\frac{\partial\widetilde{F}}{\partial\eta}+\frac{\partial\widetilde{G}}{\partial\zeta}=0, \tag{3.1}$$

and their semi-discrete approximation,

$$\frac{\partial\widetilde{U}}{\partial t}=-\delta_{\mathrm{I}}^{\xi}\widetilde{E}-\delta_{\mathrm{I}}^{\eta}\widetilde{F}-\delta_{\mathrm{I}}^{\zeta}\widetilde{G}. \tag{3.2}$$

The discretization $\delta_{\mathrm{I}}^{\xi}$, $\delta_{\mathrm{I}}^{\eta}$ and $\delta_{\mathrm{I}}^{\zeta}$ are the same, thus we only give the discretization in ξ direction. The $\delta_{\mathrm{I}}^{\xi}$ of the HDCS-E8T7 is

$$\begin{aligned} \delta_{\mathrm{I}}^{\xi}\widetilde{E}_j=&\frac{256}{175h}\left(\hat{E}_{j+1/2}-\hat{E}_{j-1/2}\right)-\frac{1}{4h}\left(\widetilde{E}_{j+1}-\widetilde{E}_{j-1}\right) \\ &+\frac{1}{100h}\left(\widetilde{E}_{j+2}-\widetilde{E}_{j-2}\right)-\frac{1}{2100h}\left(\widetilde{E}_{j+3}-\widetilde{E}_{j-3}\right), \end{aligned} \tag{3.3}$$

where, $\hat{E}_{j\pm1/2}=\widetilde{E}(\hat{U}_{j\pm1/2},\hat{\xi}_{x,j\pm1/2},\hat{\xi}_{y,j\pm1/2},\hat{\xi}_{z,j\pm1/2})$ and $\widetilde{E}_{j+m}=\widetilde{E}(U_{j+m},\hat{\xi}_{x,j\pm m},\hat{\xi}_{y,j\pm m},\hat{\xi}_{z,j\pm m})$ are the fluxes at cell edges and at cell nodes, respectively. The numerical flux $\hat{E}_{j\pm1/2}$ is evaluated by the variables at cell-edges,

$$\hat{E}_{j\pm1/2}=\widetilde{E}\left(\hat{U}^L_{j\pm1/2},\hat{U}^R_{j\pm1/2},\hat{\xi}_{x,j\pm1/2},\hat{\xi}_{y,j\pm1/2},\hat{\xi}_{z,j\pm1/2}\right), \tag{3.4}$$

https://doi.org/10.4208/aamm.2014.m459 Published online by Cambridge University Press

where, $\hat{U}^L_{j\pm1/2}$, $\hat{U}^R_{j\pm1/2}$ are variables at cell-edge,

$$\begin{aligned}&\frac{5}{14}(1-\alpha)\hat{U}^L_{j-1/2}+\hat{U}^L_{j+1/2}+\frac{5}{14}(1+\alpha)\hat{U}^L_{j+3/2}\\&=\frac{25}{32}(U_{j+1}+U_j)+\frac{5}{64}(U_{j+2}+U_{j-1})-\frac{1}{448}(U_{j+3}+U_{j-2})\\&\quad+\alpha\left[\frac{25}{64}(U_{j+1}-U_j)+\frac{15}{128}(U_{j+2}-U_{j-1})-\frac{5}{896}(U_{j+3}-U_{j-2})\right],\end{aligned}\tag{3.5}$$

where $\alpha<0$ is the dissipative parameter controlling the dissipation of the HDCS-E8T7. The corresponding $\hat{U}^R_{j+1/2}$ can be obtained easily by setting $\alpha>0$. Dissipative parameter α has no influence on the accuracy of the HDCS-E8T7 scheme, however, it has effect on resolution of the scheme. Comparing with the central compact scheme proposed by Lele [7], Fig. 1 plots the modified wavenumber of the HDCS-E8T7 with different dissipative parameters. It may be noticed that the resolution of the HDCS-E8T7 is approximately spectral-like. According to the concept of Dispersion-Relation-Preserving (DRP) [31], the HDCS-E8T7 has been optimized by adjusting the value of α. The optimized dissipative parameter is equal to 0.3 [18], which will be adopted in this paper.

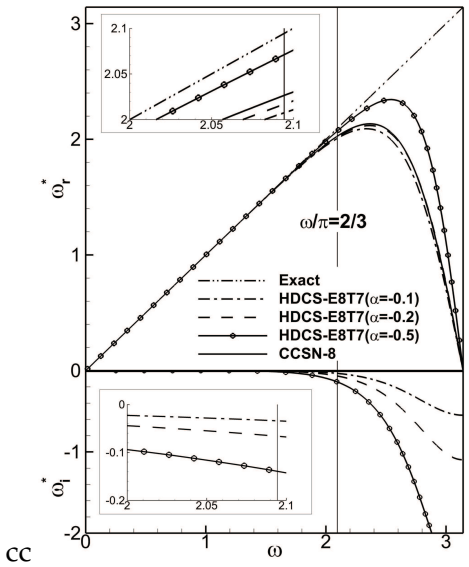


Figure 1: Modified wavenumber of the HDCS-E8T7.

Seven-point stencil is used by the HDCS-E8T7, thus three levels of boundary and near-boundary schemes are required for the left-side boundary nodes $j=1,2,3$ as well as for the right-side boundary nodes $j=N,N-1,N-2$. The sixth-order scheme is used for the near boundary $j=3$ and $j=N-2$,

$$\widetilde{E}'_j=\frac{64}{45h}(\hat{E}_{j+1/2}-\hat{E}_{j-1/2})-\frac{2}{9h}(\widetilde{E}_{j+1}-\widetilde{E}_{j-1})+\frac{1}{180h}(\widetilde{E}_{j+2}-\widetilde{E}_{j-2}).\tag{3.6}$$

https://doi.org/10.4208/aamm.2014.m459 Published online by Cambridge University Press

The fourth-order scheme is employed for the near boundary $j=2$ and $j=N-1$,

$$\widetilde{E}'_j=\frac{4}{3h}(\hat{E}_{j+1/2}-\hat{E}_{j-1/2})-\frac{1}{6h}(\widetilde{E}_{j+1}-\widetilde{E}_{j-1}). \tag{3.7}$$

The fourth-order boundary schemes for $j=1$ and $j=N$ are

$$\widetilde{E}'_1=\frac{1}{6h}(48\hat{E}_{3/2}+16\hat{E}_{5/2}-25\widetilde{E}_1-36\widetilde{E}_2-3\widetilde{E}_3), \tag{3.8a}$$

$$\widetilde{E}'_N=\frac{-1}{6h}(48\hat{E}_{N-1/2}+16\hat{E}_{N-3/2}-25\widetilde{E}_N-36\widetilde{E}_{N-1}-3\widetilde{E}_{N-2}). \tag{3.8b}$$

For boundary schemes, the fifth-order interpolations for $j=3/2$ and $j=N-1/2$ are

$$\hat{U}^L_{3/2}=\frac{1}{128}(35U_1+140U_2-70U_3+28U_4-5U_4), \tag{3.9a}$$

$$\hat{U}^L_{N-1/2}=\frac{1}{128}(35U_N+140U_{N-1}-70U_{N-2}+28U_{N-3}-5U_{N-4}), \tag{3.9b}$$

synchronously, the fifth-order dissipative compact interpolations for $j=5/2$ and $j=N-3/2$ are given by

$$\begin{aligned}&\frac{3}{10}(1-\alpha)\hat{U}^L_{j-1/2}+\hat{U}^L_{j+1/2}+\frac{3}{10}(1+\alpha)\hat{U}^L_{j+3/2}\\&=\frac{3}{4}(U_{j+1}+U_j)+\frac{1}{20}(U_{j+2}+U_{j-1})+\alpha\Big[\frac{3}{8}(U_{j+1}-U_j)+\frac{3}{40}(U_{j+2}-U_{j-1})\Big].\end{aligned} \tag{3.10}$$

For the computation of the viscous terms, the primitive variables, u, v, w, T, are first differentiated to form the components of the stress tensor and the heat flux vector. The viscous flux derivatives are then computed by a second application of the HDCS-E8T7.

3.2 Time integration

For the test of scattering of acoustic waves by multiple cylinder, the equations are integrated in time with the fifth-order five-stage Runge-kutta scheme [32]. With R denoting the residual, the governing equation is

$$\frac{\partial\widetilde{U}}{\partial t}=R=\frac{\theta}{R_e}\Big(\frac{\partial\widetilde{E}_v}{\partial\xi}+\frac{\partial\widetilde{F}_v}{\partial\eta}+\frac{\partial\widetilde{G}_v}{\partial\zeta}\Big)+\frac{\overrightarrow{S}}{J}-\frac{\partial\widetilde{E}}{\partial\xi}-\frac{\partial\widetilde{F}}{\partial\eta}-\frac{\partial\widetilde{G}}{\partial\zeta}. \tag{3.11}$$

The fifth-order five-stage Runge-kutta scheme integrates from time t_0 (step n) to $t_0+\Delta t$ (step $n+1$) through the operations

$$R^1=\Delta tR(\widetilde{U}^n),\qquad R^2=\Delta tR\Big(\widetilde{U}^n+\frac{1}{5}\Delta tR^1\Big),\quad R^3=\Delta tR\Big(\widetilde{U}^n+\frac{1}{4}\Delta tR^2\Big), \tag{3.12a}$$

$$R^4=\Delta tR\Big(\widetilde{U}^n+\frac{1}{3}\Delta tR^3\Big),\quad R^5=\Delta tR\Big(\widetilde{U}^n+\frac{1}{2}\Delta tR^4\Big),\quad \widetilde{U}^{n+1}=\widetilde{U}^n+R^5. \tag{3.12b}$$

https://doi.org/10.4208/aamm.2014.m459 Published online by Cambridge University Press

For numerical test on rod-airfoil configuration, the computational mesh is highly stretched. The stability constraint of explicit time-marching methods is too restrictive and the use of an implicit approach becomes necessary, then dual time stepping scheme [33] with Newton-like sub-iterations [34] is employed. The second-order dual time stepping scheme may be written as

$$\left[J^{-1}\left(\frac{1}{\Delta\tau}+\frac{3}{2\Delta t}\right)I+\mathrm{M}(U^p)\right]\Delta U^{p+1}=-\left[J^{-1}\frac{3U^p-4U^n+U^{n-1}}{2\Delta t}+R(U^p)\right], \tag{3.13}$$

where $\mathrm{M}(U)=\partial R(U)/\partial U$, and τ is pseudo-time. For the first sub-iteration, $p=1$, $U^p=U^n$, and as $p\to\infty$, $U^p\to U^{n+1}$. The spatial derivatives in the implicit operators are represented using standard second-order approximations whereas seventh-order discretizations are employed for the residual.

3.3 Calculation of the grid metric derivatives

According to the study of Deng et al. [15], the SCL is satisfied automatically on uniform meshes. However, the SCL may be dissatisfied on curvilinear meshes. If the SCL has not been satisfied, numerical instabilities and even computing collapse may appear on complex curvilinear grids during numerical simulation. In this subsection, we will discuss the calculation of the grid metric derivatives according to the principle of satisfying the SCL on curvilinear meshes. The conservative grid metric derivatives Eq. (2.2) have the discretization form as

$$\begin{cases}
\tilde{\xi}_x=\delta^{\zeta}_{\mathrm{II}}((\delta^{\eta}_{\mathrm{III}}y)z)-\delta^{\eta}_{\mathrm{II}}((\delta^{\zeta}_{\mathrm{III}}y)z), & \tilde{\xi}_y=\delta^{\zeta}_{\mathrm{II}}((\delta^{\eta}_{\mathrm{III}}z)x)-\delta^{\eta}_{\mathrm{II}}((\delta^{\zeta}_{\mathrm{III}}z)x), & \tilde{\xi}_z=\delta^{\zeta}_{\mathrm{II}}((\delta^{\eta}_{\mathrm{III}}x)y)-\delta^{\eta}_{\mathrm{II}}((\delta^{\zeta}_{\mathrm{III}}x)y),\\
\tilde{\eta}_x=\delta^{\xi}_{\mathrm{II}}((\delta^{\zeta}_{\mathrm{III}}y)z)-\delta^{\zeta}_{\mathrm{II}}((\delta^{\xi}_{\mathrm{III}}y)z), & \tilde{\eta}_y=\delta^{\xi}_{\mathrm{II}}((\delta^{\zeta}_{\mathrm{III}}z)x)-\delta^{\zeta}_{\mathrm{II}}((\delta^{\xi}_{\mathrm{III}}z)x), & \tilde{\eta}_z=\delta^{\xi}_{\mathrm{II}}((\delta^{\zeta}_{\mathrm{III}}x)y)-\delta^{\zeta}_{\mathrm{II}}((\delta^{\xi}_{\mathrm{III}}x)y),\\
\tilde{\zeta}_x=\delta^{\eta}_{\mathrm{II}}((\delta^{\xi}_{\mathrm{III}}y)z)-\delta^{\xi}_{\mathrm{II}}((\delta^{\eta}_{\mathrm{III}}y)z), & \tilde{\zeta}_y=\delta^{\eta}_{\mathrm{II}}((\delta^{\xi}_{\mathrm{III}}z)x)-\delta^{\xi}_{\mathrm{II}}((\delta^{\eta}_{\mathrm{III}}z)x), & \tilde{\zeta}_z=\delta^{\eta}_{\mathrm{II}}((\delta^{\xi}_{\mathrm{III}}x)y)-\delta^{\xi}_{\mathrm{II}}((\delta^{\eta}_{\mathrm{III}}x)y),
\end{cases} \tag{3.14}$$

where $\delta^{\xi}_{\mathrm{II}}$, $\delta^{\eta}_{\mathrm{II}}$, $\delta^{\zeta}_{\mathrm{II}}$ and $\delta^{\xi}_{\mathrm{III}}$, $\delta^{\eta}_{\mathrm{III}}$, $\delta^{\zeta}_{\mathrm{III}}$ are numerical derivative operators used for the metric calculations in ξ, η and ζ coordinate directions, respectively. For the applications on curvilinear meshes, finite difference scheme should satisfy the SCL which means $I_x=I_y=I_z=0$ [15],

$$\begin{cases}
I_x=\delta^{\xi}_{\mathrm{I}}(\tilde{\xi}_x)+\delta^{\eta}_{\mathrm{I}}(\tilde{\eta}_x)+\delta^{\zeta}_{\mathrm{I}}(\tilde{\zeta}_x),\\
I_y=\delta^{\xi}_{\mathrm{I}}(\tilde{\xi}_y)+\delta^{\eta}_{\mathrm{I}}(\tilde{\eta}_y)+\delta^{\zeta}_{\mathrm{I}}(\tilde{\zeta}_y),\\
I_z=\delta^{\xi}_{\mathrm{I}}(\tilde{\xi}_z)+\delta^{\eta}_{\mathrm{I}}(\tilde{\eta}_z)+\delta^{\zeta}_{\mathrm{I}}(\tilde{\zeta}_z).
\end{cases} \tag{3.15}$$

In order to fulfill the SCL, the grid metrics should be calculated with a conservative form by the same schemes used for flux derivative calculations, i.e., $\delta_{\mathrm{I}}=\delta_{\mathrm{II}}$, to implement the CMM [15]. It has been proved in [15] that the CMM can be easily applied in high-order schemes if the difference operator δ_{I} of flux derivatives is not split, while it is difficult to be applied in the schemes where the δ_{I} is split into two upwind operators as δ^{+}_{I} and δ^{-}_{I}. Although the inner-level difference operators δ_{III} in the conservative metrics have no effect on the GCL, the constraint $\delta_{\mathrm{III}}=\delta_{\mathrm{II}}$ is recommended by Deng et al. [15]. More recently, the constraint $\delta_{\mathrm{III}}=\delta_{\mathrm{II}}$ is explained from geometry viewpoint, and the

https://doi.org/10.4208/aamm.2014.m459 Published online by Cambridge University Press

symmetrical conservative metric method (SCMM) [35], which can evidently increase the numerical accuracy on irregular grids is proposed. To eliminate the SCL errors on curvilinear mesh, here we calculate the grid metrics with a conservative form by the same schemes used for flux derivative calculations, i.e., $\delta_{\rm I}=\delta_{\rm II}=\delta_{\rm III}$. Then explicit eighth-order central interpolation is employed for $\delta_{\rm II}$ and $\delta_{\rm III}$ at interior nodes,

$$\begin{aligned}\hat{U}_{j+1/2}=&\frac{1}{2048}(1225(U_{j+1}+U_j)-245(U_{j+2}+U_{j-1})\\&+49(U_{j+3}+U_{j-2})-5(U_{j+4}+U_{j-3})).\end{aligned}\tag{3.16}$$

At boundary points, the interpolations for $\delta_{\rm II}$ and $\delta_{\rm III}$ are

$$\hat{U}_{3/2}=\frac{1}{128}(35U_1+140U_2-70U_3+28U_4-5U_5),\tag{3.17a}$$

$$\hat{U}_{5/2}=\frac{1}{128}(-5U_1+60U_2+90U_3-20U_4+3U_5),\tag{3.17b}$$

$$\hat{U}_{7/2}=\frac{1}{256}(3U_1-25U_2+150U_3+150U_4-25U_5+3U_6),\tag{3.17c}$$

$$\hat{U}_{N-1/2}=\frac{1}{128}(35U_N+140U_{N-1}-70U_{N-2}+28U_{N-3}-5U_{N-4}),\tag{3.17d}$$

$$\hat{U}_{N-3/2}=\frac{1}{128}(-5U_N+60U_{N-1}+90U_{N-2}-20U_{N-3}+3U_{N-4}),\tag{3.17e}$$

$$\hat{U}_{N-5/2}=\frac{1}{256}(3U_N-25U_{N-1}+150U_{N-2}+150U_{N-3}-25U_{N-4}+3U_{N-5}).\tag{3.17f}$$

4 Numerical tests

In this section, we will investigate the performance of the HDCS-E8T7 for aeroacoustic prediction on curvilinear meshes. A benchmark problem is used to demonstrate the high resolution of the HDCS-E8T7 for aeroacoustic prediction on curvilinear meshes, and then this aeroacoustic prediction method based on the HDCS-E8T7 is used to handle the realistic rod-airfoil configuration including multiple solid bodies. For the aeroacoustic prediction in the far-field, the Ffowcs Williams-Hawkings (FW-H) integral method [36] is employed. Finally, subsonic jet noise from nozzle is predicted.

4.1 Scattering of acoustic waves by multiple cylinder

The case examined here is specified in Category 2 of the Fourth Computational Aeroacoustics Workshop on Benchmark Problems. The source term on the right-hand side of Euler equations (2.1) is applied to the energy equation only, it is specified as

$$S=\exp[-2\ln 2(x^2+y^2)]\sin(8\pi t).\tag{4.1}$$

A cubic ramping function is added to the above Eq. (4.1) to gradually introduce the source into computational domain over some finite amount of time at the beginning of

https://doi.org/10.4208/aamm.2014.m459 Published online by Cambridge University Press

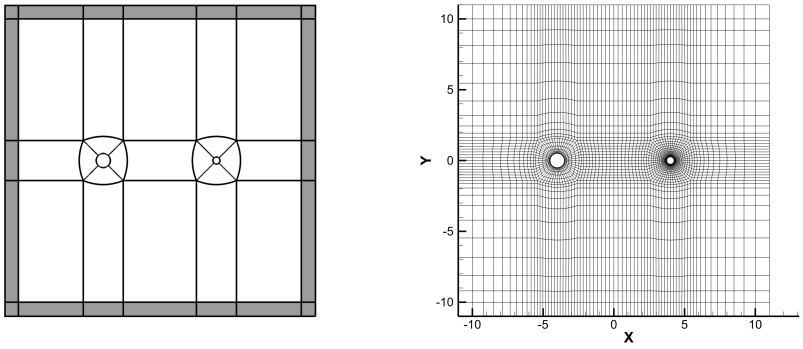


Figure 2: Computed domain and mesh of two-cylinder scattering case.

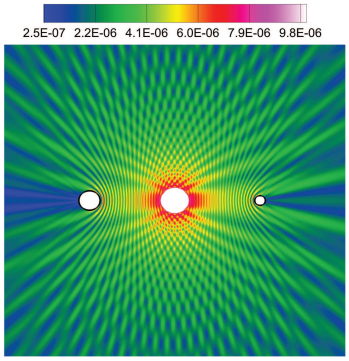


Figure 3: Root-mean-square value of the fluctuating pressure.

the computation. At the solid surfaces, the physical velocity components are found from the contravariant velocity components by setting $V=\eta_x u+\eta_y v+\eta_z w$ at the surface equal to zero and extrapolating for $U=\xi_x u+\xi_y v+\xi_z w$ on the surface using a fifth-order formulation. The pressure and density at the wall are also calculated by using the fifth-order extrapolation. At the far-field boundaries, sponge technique [37] is employed. The solutions are advanced with the time step of 0.002 (125 time steps per source period) for total 20,000 time steps, with mean values computed over the last 2,000 time steps. Fig. 2 shows the computational domain. Three meshes have been used to solve this problem. The numbers of the 2D grid points are 469×409 (coarse), 721×685 (medium), 841×775 (fine).

Fifth-order five-stage Runge-kutta scheme [32] is used for the time integration, the HDCS-E8T7 is employed to calculate numerical flux derivatives. Fig. 3 plots the root-mean-square (RMS) value of the fluctuating pressure calculated by the HDCS-E8T7. A diffraction field is generated by the acoustic waves coming from the source, and the silent zone behind the cylinder can be observed. In Fig. 4, the RMS value of the fluctuating pressure on the surface of the cylinders calculated by the HDCS-E8T7 on the three meshes

https://doi.org/10.4208/aamm.2014.m459 Published online by Cambridge University Press

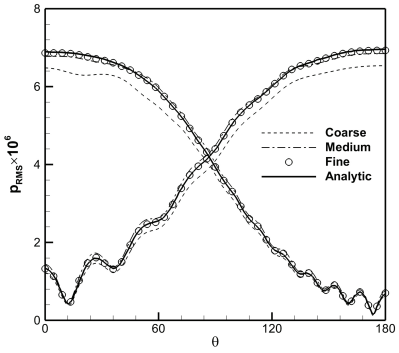


Figure 4: RMS fluctuating pressure on the surface of cylinders.

are plotted. Numerical solution approaches the analytic solution as the number of grid points increase. On the fine mesh, excellent agreement between the analytic and the numerical solutions has been acquired. It manifests high resolution of the HDCS-E8T7 for aeroacoustic prediction.

4.2 Sound radiated by a rod-airfoil configuration

This case is used to test the ability of the HDCS-E8T7 for aeroacoustic noise prediction on complex geometry. The numerical results will be compared to experimental data of the rod-airfoil reported by Jacob et al. [38]. Computations are conducted for the same conditions as in the experiment, where the incoming Mach number is $M=0.2$, chord length of the NACA0012 airfoil is $c=0.1$m, and the corresponding chord Reynolds number is 4.8×10^5. The airfoil is located one chord downstream of a rod (diameter: $d=0.1\times c$). In this configuration, the rod wake that impinges the airfoil contains both periodic and broadband turbulent disturbances. For the simulation of turbulent flow which has the main responsibility for the noise radiated by this rod-airfoil configuration, the HILES [21] based on the HDCS-E8T7 is employed. The far-field noise is calculated by applying the Ffowcs-Williams and Hawking aeroacoustic analogy [36] to the FW-H integration surface, and no volume integration is performed.

Fig. 5 outlines the computational domain, which contains approximately 16,000,000 grid points. For the comparison following, the sketch of locations in the measurement of Jacob et al. [38] is also shown in this figure. The grid extends $3d$ in spanwise direction, and the 2D grid is reproduced in span direction with 45 cells. Grid points are clustered near the rod and airfoil surfaces, with the minimum normal spacing of 1.0×10^{-5} (normalized by the reference length $L_{ref}=0.1$m). Highly stretched meshes are used in this test, then dual time stepping scheme [33] with Newton-like subiterations [34] is employed for the time integration. At the outer boundaries, far-field boundary conditions based on the LODI approximation [39] and sponge technique [37] are prescribed. The no-slip condition is invoked on the rod and airfoil surfaces, together with fifth-order accurate

https://doi.org/10.4208/aamm.2014.m459 Published online by Cambridge University Press

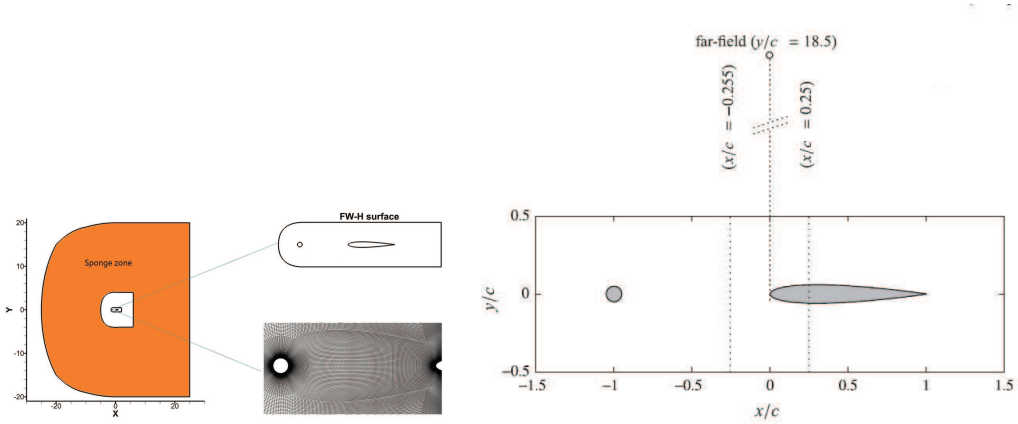


Figure 5: Sectional view of the computational domain (left) and sketch of the locations for the measurements (right).

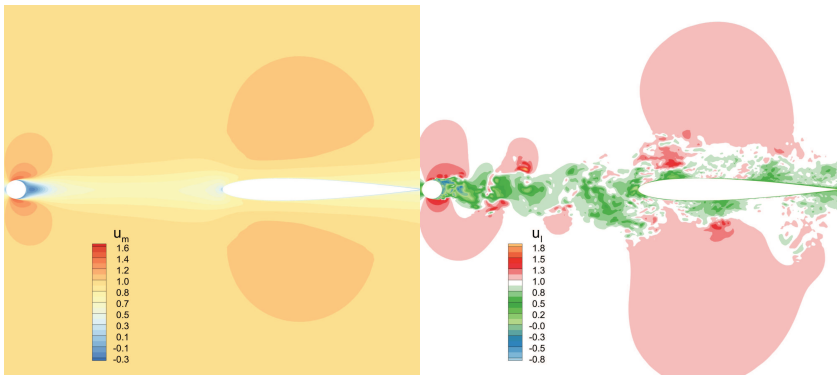


Figure 6: Mean (left) and instantaneous (right) streamwise velocity contours.

approximations for the adiabatic wall and zero normal pressure gradient. At the spanwise boundaries, periodicity condition is applied. The computations are advanced for total 30,000 time steps, and flow statistics are collected for the last 20,000 time steps. For periodic boundaries in the spanwise directions, flow statistics are averaged in z-direction.

To depict the flow field calculated by the HILES, Fig. 6 plots the mean and instantaneous streamwise (taken in the central plane of the computational domain) velocity contours. It can be seen that the von Kármán vortices in the rod wake impinge onto the airfoil, and then partly split at the leading edge. Furthermore, many smaller structures can be found in the rod turbulent wake. This multiple scale flow is dominated by the main vortices which is the major feature of the rod-airfoil configuration. Comparing with the experimental measurements [38], Fig. 7 shows the mean velocity normalized by incoming velocity at two locations $x/c=-0.255$ and $x/c=0.25$. At the location $x/c=-0.255$, the mean streamwise velocity near the center-line is under-predicted, which is consistent with the over-prediction of the mean streamwise velocity near the wall at location

https://doi.org/10.4208/aamm.2014.m459 Published online by Cambridge University Press

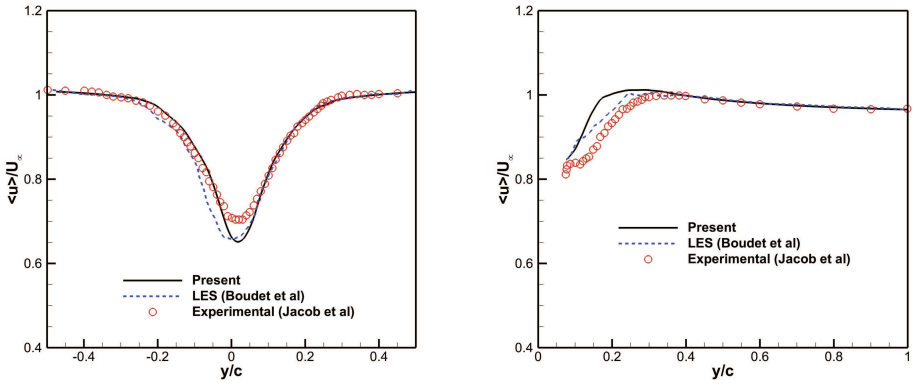


Figure 7: Spanwise averaged mean streamwise velocity distributions at locations $x/c=-0.255$ (left) and $x/c=0.25$ (right).

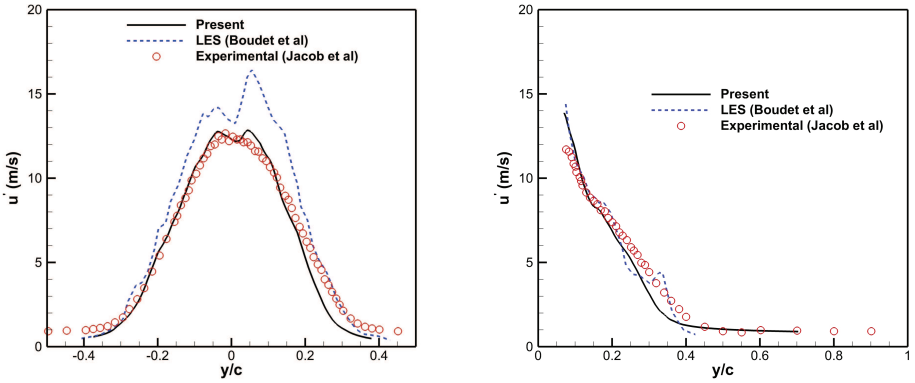


Figure 8: Spanwise averaged RMS value of fluctuating velocity at locations $x/c=-0.255$ (left) and $x/c=0.25$ (right).

$x/c=0.25$ since the flow predicted moves more slowly between the rod and airfoil. The similar phenomenon is observed from the LES prediction of Boudet et al. [40]. Moreover, as shown in Fig. 8, the predicted profiles of the RMS value of streamwise velocity at two locations $x/c=-0.255$ and $x/c=0.25$ have good agreement with that from experimental data. This seems to indicate that the turbulence intensities are well predicted by the HILES. Another evidence demonstrating the reliability of the HILES is the resolved energy spectrum behind the cylinder, which is given in Fig. 9. The resolved scales seem to reach an inertial subrange, reasonably close to $St^{-5/3}$ scaling [41]. St is the characteristic Strouhal number defined as $St=fd/U_\infty$ with f being the frequency and U_∞ being the incoming velocity. The illustrated slope indicates that the HILES can reliably capture the turbulence spectrum. Fig. 10 plots the iso-surface of the second invariant colored by density contours. The second invariant Q is

$$Q=(\Omega_{ij}\Omega_{ij}+S_{ij}S_{ij})/2, \tag{4.2}$$

https://doi.org/10.4208/aamm.2014.m459 Published online by Cambridge University Press

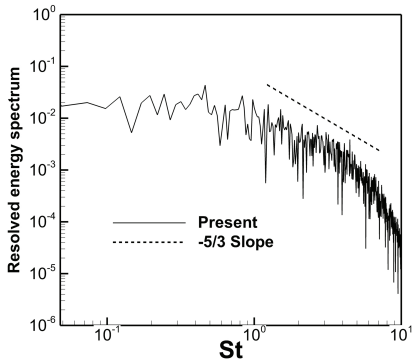


Figure 9: Resolved energy spectrum at a location behind the cylinder.

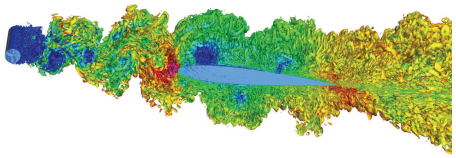


Figure 10: Iso-surfaces of the second invariant of velocity gradient tensor for instantaneous vortex structure.

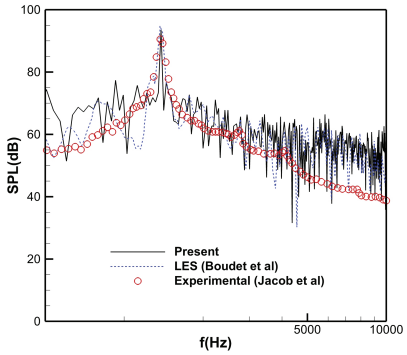


Figure 11: The SPL spectra at the location ($x=0.68$m, $y=1.74$m) calculated from the pressure perturbations.

where $\Omega_{ij}=(u_{i,j}-u_{j,i})/2$ and $S_{ij}=(u_{i,j}+u_{j,i})/2$ are the antisymmetric and the symmetric components of the curl of the velocity, respectively. Due to the fine resolution of the HDCS-E8T7, we may see the details about the vortex structure. In Fig. 11, we present the sound pressure level (SPL) spectra at the location ($x=0.68$m, $y=1.74$m) calculated from the pressure fluctuations on the FW-H integration surface. The HILES predicts quite well the peak frequency. Furthermore, the broadband spectrum is also well described around the peak frequency. However, the spectrum on high frequencies is over-predicted, which is similar to the LES results of Boudet et al. [40]. A possible explanation given by Boudet et al. [40] for this phenomenon is that the dipole cancellation of some quadrupole terms may be momentarily ineffective which could lead to more efficient sources. Nevertheless, the good broadband sound is predicted by the HILES.

https://doi.org/10.4208/aamm.2014.m459 Published online by Cambridge University Press

4.3 Jet noise from nozzle

The nozzle considered here is the same as the one studied by Andersson et al. [42].The diameter D_j of the nozzle is $50mm$. The Reynolds number based on the nozzle exit diameter and the jet velocity at the nozzle exit plane, Re_D is 5.0×10^4. The acoustic Mach number is $M_a=0.75$. Simulation has been performed for the jet with exit static temperature T_j equaling to the ambient temperature T_∞, the inlet conditions for the simulated jet are the same as that used by Tide et al. [43].

The computational domain used for the three-dimensional simulation is given in Fig. 12. In order to minimize the effect of reflections at the domain outlet and far-field on the predicted flow field, the sponge zone [37] is added at the domain outlet and far-field. The domain extends 20 nozzle diameters downstream of the nozzle exit. The diameter of the domain at the inlet is $10D_j$, at the outlet is $20D_j$ and the length of sponge zone is $40D_j$. The computational domain is discretized using a multi-block structured mesh with about 1.8×10^8 cells. The computational mesh system is shown in Fig. 13.

At nozzle inlet, the static and stagnation pressure are specified. At the domain outlet, i.e., at the downstream end of the sponge layer, static pressure is specified. For all free boundaries, far-field boundary conditions based on the LODI approximation [39] and sponge technique [37] are prescribed. The no-slip condition is invoked on the nozzle

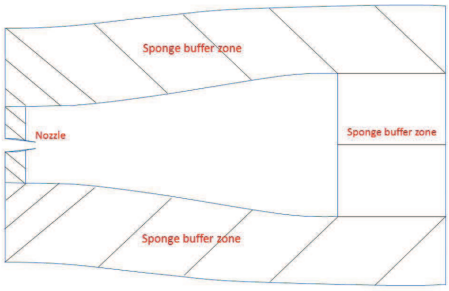
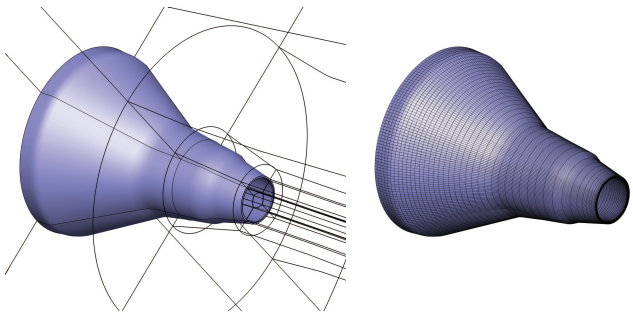


Figure 12: Sectional view of the computational domain.



(a) Grid topology (b) Grid on the solid wall

Figure 13: Mesh system for the nozzle.

https://doi.org/10.4208/aamm.2014.m459 Published online by Cambridge University Press

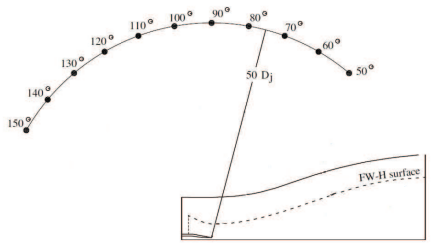


Figure 14: Locations of the far-field receivers.

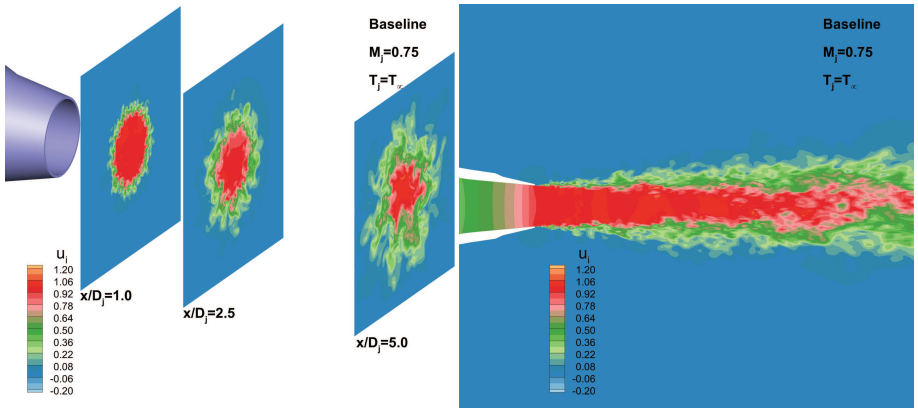


Figure 15: Contours of instantaneous axial velocity.

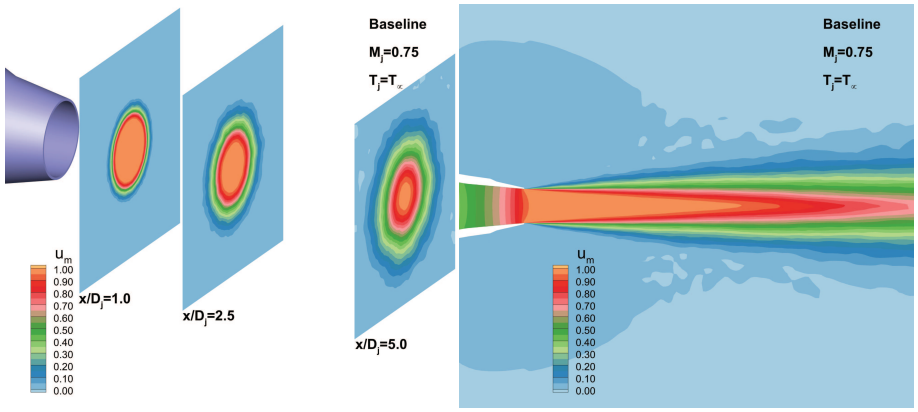


Figure 16: Contours of mean axial velocity.

surface, together with fifth-order accurate approximations for the adiabatic wall and zero normal pressure gradient.

The HILES based on the HDCS-E8T7 is used to predict the aerodynamic sources of the jet noise in turbulence flow, however, is not suited for acoustic propagation due to the dif-

https://doi.org/10.4208/aamm.2014.m459 Published online by Cambridge University Press

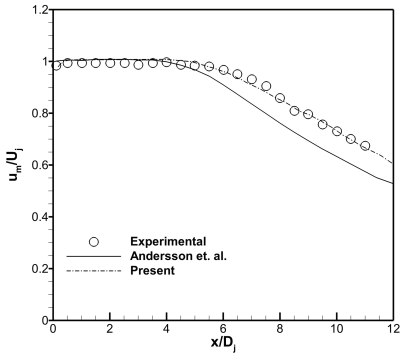


Figure 17: Distributions of axial velocity along the centerline.

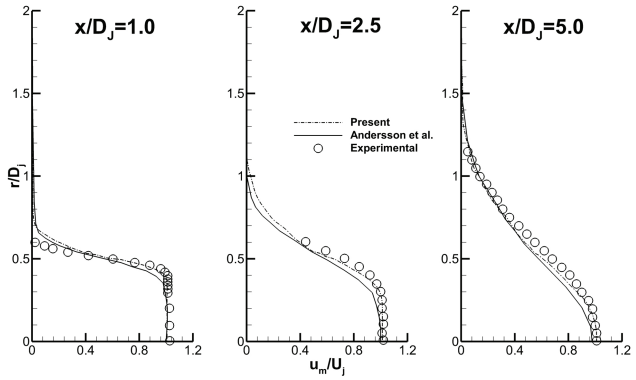


Figure 18: Radial profile of velocity at different axial locations.

ferent numerical requirements of the aerodynamic and acoustic computations, especially the efficiency. For the aeroacoustic prediction in the far-field, the FW-H integral method is employed to calculate the far-field fluctuating acoustic pressure. Initially, steady state calculations are run until the overall mass balance in the domain is less than 1% of the mass flow rate through the nozzle. Then unsteady calculations are started. The computation is advanced with the time step $\Delta t = 4\mu s$ for total 30,000 time steps, and flow statistics are collected for the last 20,000 time steps. The fluctuating acoustic pressure at several receiver locations are then calculated using the FW-H integral method [36]. These receiver locations are shown in Fig. 14. The time history of the pressure on the FW-H surface is used as the input for the acoustic calculation. This surface is chosen large enough to enclose all the acoustic sources, in this case, the shear layer.

To depict the flow field calculated by the HILES, Figs. 15 and 16 plot the instantaneous and mean axial velocity contours, respectively. In Fig. 17, profile of mean axial velocity along the center-line is compared with the computational and experimental data reported by Andersson et al. [42]. It is shown that the potential core length, as well as the decay of velocity after the potential core, are predicted better in the present simulation. Variation

https://doi.org/10.4208/aamm.2014.m459 Published online by Cambridge University Press

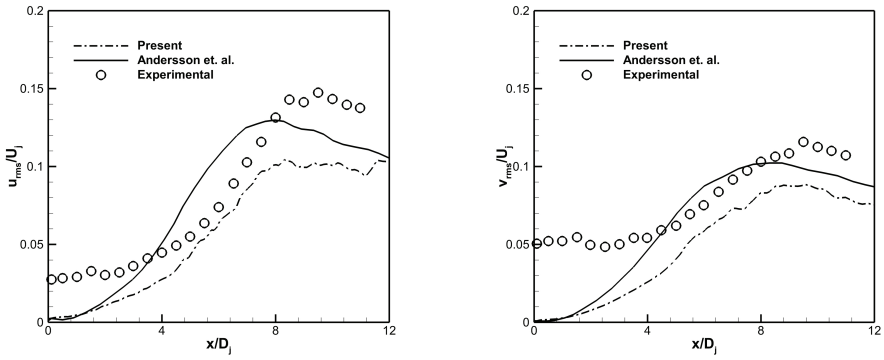


Figure 19: Variation of u_{rms} (left) and v_{rms} (right) along the centerline.

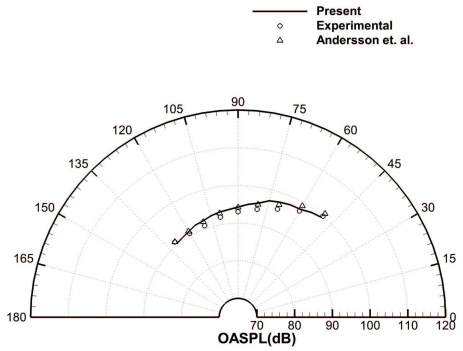


Figure 20: Sound pressure levels at observer locations.

of the axial velocity in the radial direction at three axial locations, namely, $x/D_j=1,2.5,5$ is shown in Fig. 18. Comparing with the solutions of Andersson et al. [42], our HILES predictions are in good agreement with the experimental data, especially at the locations $x/D_j=2.5,5$. Fig. 19 plots RMS values of the fluctuating velocity normalized by mean jet velocity at the nozzle exit plane. Comparing with the experimental data, the locations of the peaks in u_{rms} and v_{rms} profiles are well predicted by present investigation. However, the HILES calculations predict very low levels of turbulence in the region $x/D_j<6$, which is the location of the potential core. The same phenomenon is observed by Andersson et al. [42]. Fig. 20 shows a comparison between predicted and measured overall sound pressure levels (OASPLs) at the observer locations. Encouraging agreements between the present computational data and experimental data [42] can be observed.

5 Conclusions

The performance of the HDCS-E8T7 has been investigated using three typical cases on multi-block structured meshes for aeroacoustic prediction in subsonic flow. According

https://doi.org/10.4208/aamm.2014.m459 Published online by Cambridge University Press

to the solutions of the scattering of acoustic waves by multiple cylinder, it is clear that the HDCS-E8T7 has high resolution for the aeroacoustic prediction. Numerical results of the sound radiated from a rod-airfoil configuration indicate that the HILES based on the HDCS-E8T7 can reliably capture the noise radiated by turbulent flow, and the potential of the HDCS-E8T7 for aeroacoustic prediction on complex geometry is shown. Comparing with the LES results and experimental measurements, the mean velocity as well as RMS profiles of streamwise velocity given by the HILES are reasonable. The reliability of the HILES is also demonstrated by the illustrated slope of resolved energy spectrum behind the cylinder. For the jet noise prediction, the present computational results show encouraging agreement with the measurements. The potential core length, as well as the decay of velocity after the potential core, are predicted well in the present simulation. Furthermore, predicted sound pressure levels are in excellent agreement with the experimental data.

The HDCS-E8T7, which can satisfy the GCL and has good performance in simulating three typical aeroacoustic problems, is further expected to successfully predict aeroacoustic noise on complex geometry. In the future, more efforts will be done to show the ability of the HDCS-E8T7 in handling aeroacoustic problems on complex geometry.

Acknowledgments

This study was supported by National Natural Science Foundation of China (Grant Nos. 11072259 and 11202226).

References

[1] M. Wang, J. B. Freund, and S. K. Lele, *Computational prediction of flow-generated sound,* Annu. Rev. Fluid Mech., 38 (2006), pp. 483–512.
[2] P. Jordan and T. Colonius, *Wave packets and turbulent jet noise*, Annu. Rev. Fluid Mech., 45 (2013), pp. 175–195.
[3] C. K. W. Tam, *Recent advances in computational aeroacoustics,* Fluid Dyn. Research, 38 (2006), pp. 591–615.
[4] T. Colonius and S. K. Lele, *Computational aeroacoustics: progress on nonlinear problems of sound generation*, Progress in Aerospace Sciences, 40 (2004), pp. 345–416.
[5] U. Paliath, H. Shen, R. Avancha and C. Shieh, *Large eddy simulation for jets from chevron and dual flow nozzles,* AIAA Paper 2011-2881.
[6] C. Bailly, C. Bogey, and O. Marsden, *Progress in direct noise computation*, Int. J. Aeroacoustics, 9 (2010), pp. 123–143.
[7] S. K. Lele, *Compact finite difference schemes with spectral-like resolution,* J. Comput. Phys., 103 (1992), pp. 16–42.
[8] F. Daude, J. Berland, T. Emmert, P. Lafon, F. Crouzet and C. Bailly, *A high-order finite-difference algorithm for direct computation of aerodynamic sound,* Comput. Fluids, 61 (2012), pp. 46–63.

https://doi.org/10.4208/aamm.2014.m459 Published online by Cambridge University Press

[9] D. P. Rizzetta, M. R. Visbal and P. E. Morgan, *A high-order compact finite-difference scheme for large-eddy simulation of active flow control,* Progress in Aerospace Sciences, 44 (2008), pp. 397–426.
[10] Z. J. Wang, *High-order methods for the Euler and Navier-Stokes equations on unstructured grids,* Progress in Aerospace Sciences, 43 (2007), pp. 1–41.
[11] J. A. Ekaterinaris, *High-order accurate, low numerical diffusion methods for aerodynamics,* Progress in Aerospace Sciences, 41(3-4) (2005), pp. 192–300.
[12] T. Nonomura, N. Iizuka and K. Fujii, *Freestream and vortex preservation properties of high-order WENO and WCNS on curvilinear grids,* Comput. Fluids, 39 (2010), pp. 197–214.
[13] P. D. Thomas and C. K. Lombard, *Geometric conservation law and its application to flow computations on moving grids,* AIAA J., 17(10) (1979), pp. 1030–1037.
[14] T. H. Pulliam and J. L. Steger, *On implicit finite-difference simulations of three-dimensional flow,* AIAA Paper 78-10.
[15] X. G. Deng, M. L. Mao, G. H. Tu, H. Y. Liu and H. X. Zhang, *Geometric conservation law and applications to high-order finite difference schemes with stationary grids,* J. Comput. Phys., 230 (2011), pp. 1100–1115.
[16] R. M. Visbal and D. V. Gaitonde, *On the use of higher-order finite-difference schemes on curvilinear and deforming meshes,* J. Comput. Phys., 181 (2002), pp. 155–185.
[17] X. G. Deng, Y. Jiang, M. L. Mao, H. Y. Liu and G. H. Tu, *Developing hybrid cell-edge and cell-node dissipative compact scheme for complex geometry flows,* Sci. China Tech. Sci., 56 (2013), pp. 2361–2369.
[18] X. G. Deng, Y. Jiang, M. L. Mao, H. Y. Liu, S. Li and G. H. Tu, *A family of hybrid cell-edge and cell-node dissipative compact schemes satisfying geometric conservation law,* Comput. Fluids, 116 (2015), pp. 29–45
[19] X. G. Deng, M. L. Mao, G. H. Tu, Y. F. Zhang and H. X. Zhang, *Extending weighted compact nonlinear schemes to complex grids with characteristic-based interface conditions,* AIAA J., 48(12) (2010), pp. 2840–2851.
[20] G. H. Tu, X. G. Deng and M. L. Mao, *Implementing high-order weighted compact nonlinear scheme on patched grids with a nonlinear interpolation,* Comput. Fluids, 77 (2013), pp. 181–193.
[21] Y. Jiang, M. L. Mao, X. G. Deng and H. Y. Liu, *Large eddy simulation on curvilinear meshes using seventh-order dissipative compact scheme,* Comput. Fluids, 104 (2014), pp. 73–84.
[22] J. P. Boris, F. F. Grinstein, E. S. Oran and R. L. Kolbe, *New insights into large eddy simulation,* Fluid Dyn. Res., 10 (1992), pp. 199–228.
[23] Y. Jiang, M. L. Mao, X. G. Deng and H. Y. Liu, *Effect of surface conservation law on large eddy simulation based on seventh-order dissipative compact scheme,* Appl. Mech. Mater., 419 (2013), pp. 30–37.
[24] Y. Jiang, M. L. Mao, X. G. Deng and H. Y. Liu, *Extending seventh-order dissipative compact scheme satisfying geometric conservation law to large eddy simulation on curvilinear grids,* Adv. Appl. Math. Mech., 7(2) (2015), pp. 1–23.
[25] Y. Jiang, M. L. Mao, X. G. Deng, H. Y. Liu, S. Li and Zh. G. Yan, *Extending seventh-order hybrid cell-edge and cell-node dissipative compact scheme to complex grids,* The 4th Asian Symposium on Computational Heat Transfer and Fluid Flow, Hong Kong, 3-6 June 2013.
[26] X. G. Deng, H. Maekawa and Q. Shen, *A class of high-order dissipative compact schemes,* AIAA paper, 1996-1972.
[27] M. L. Mao and X. G. Deng, *Boundary schemes and asymptotic stability for high-order dissipative compact schemes,* Acta Aerodynamica Sinica, 18(2) (2000), pp. 165–171.
[28] M. L. Mao, X. G. Deng and S. Li, *Spectrum characteristic of dissipative compact schemes and*

https://doi.org/10.4208/aamm.2014.m459 Published online by Cambridge University Press

application to couette flow, Chinese Journal of Computational Physics, 26(3) (2009), pp. 371–377.

[29] M. L. MAO, Y. JIANG AND X. G. DENG, *Study of LDDRK schemes for DCS5 scheme,* Chinese Journal of Computational Physics, 27(2) (2010), pp. 159–167.

[30] Y. JIANG, M. L. MAO AND X. G. DENG, *Application of DCS5 scheme in CAA,* Acta Aerodynamica Sinica, 30(4) (2012), pp. 431–436.

[31] C. K. W. TAM AND J. C. WEBB, *Dispersion-relation-preserving finite difference schemes for computational acoustics,* J. Comput. Phys., 107 (1993), pp. 262–281.

[32] F. Q. HU, M. Y. HUSSAINI AND J. L. MANTHEY, *Low-dissipation and low-dispersion Runge-kutta schemes for computational acoustics,* J. Comput. Phys., 124 (1996), pp. 177–191.

[33] M. H. JOHN AND A. JAMESON, *An implicit-explicit hybrid scheme for calculating complex unsteady flows,* AIAA paper, 2002-0714.

[34] R. E. GORDNIER AND M. R. VISBAL, *Numerical simulation of delta-wing roll,* AIAA Paper, 93-0554.

[35] X. G. DENG, Y. B. MIN, M. L. MAO, H. Y. LIU, G. H. TU AND H. X. ZHANG, *Further studies on geometric conservation law and applications to high-order finite difference schemes with stationary grids,* J. Comput. Phys., 239 (2013), pp. 90–111.

[36] A. S. LYRINTZIS, *Surface integral methods in computational aeroacoustics–from the (CFD) near-field to the (acoustic) far-field,* Int. J. Aeroacoustics, 2(2) (2003), pp. 95–128.

[37] D. J. BODONY, *Analysis of sponge zones for computational fluid mechanics,* J. Comput. Phys., 212 (2006), pp. 681–702.

[38] M. C. JACOB, J. BOUDET, D. CASALINO AND M. MICHARD, *A rod-airfoil experiment as benchmark for broadband noise modeling,* J. Theoret. Comput. Fluid Dyn., 19(3) (2005), pp. 171–196.

[39] T. POINSOT AND S. K. LELE, *Boundary conditions for direct simulations of compressible viscous flows,* J. Comput. Phys., 101 (1992), pp. 104–129.

[40] J. BOUDET, N. GROSJEAN AND M. C. JACOB, *Wake-airfoil interaction as broadband noise source: a large-eddy simulation study,* Int. J. Aeroacoustics, 4(1) (2005), pp. 93–116.

[41] C. Y. XU, L. W. CHEN AND X. Y. LU, *Large-eddy simulation of the compressible flow past a wavy cylinder,* J. Fluid Mech., 665 (2010), pp. 238–273.

[42] N. ANDERSSON, L. E. ERIKSSON AND L. DAVIDSON, *A study of Mach 0.75 jets and their radiated sound using large eddy simulation,* AIAA paper, 2004-3024.

[43] P. S. TIDE AND V. BABU, *Numerical predictions of noise due to subsonic jets from nozzles with and without chevrons,* Appl. Acoustics, 70 (2009), pp. 321–332.

https://doi.org/10.4208/aamm.2014.m459 Published online by Cambridge University Press